33RD CONGRESS
OF THE INTERNATIONAL COUNCIL
OF THE AERONAUTICAL SCIENCES
STOCKHOLM, SWEDEN, 4–9 SEPTEMBER, 2022

ICAS
2022
SWEDEN

EXPERIMENTAL INVESTIGATION OF A NEXT-GENERATION AIRLINER WITH BOUNDARY LAYER INGESTION

Pedro D. Bravo-Mosquera[1], João Paulo Eguea[1], Hernan D. Cerón-Muñoz[1] & Fernando M. Catalano[1]

[1]São Carlos School of Engineering - University of São Paulo (EESC-USP), São Carlos, SP, Brazil, 13563-120

Abstract

This paper describes an experimental investigation of the Boundary-Layer Ingestion (BLI) effects of a next-generation commercial airliner. The aircraft configuration integrates a box-wing layout with engines located at the rear part of the fuselage. Wind-tunnel test involved a back-to-back comparison between two aircraft models: a non-BLI version whose engines are assembled on pylons, and a BLI version to ingest the boundary-layer created over the fuselage. The experimental study included force and power measurements, flow mapping, and total pressure surveys. The results suggested that the BLI configuration enhances the propulsive efficiency by reducing both the electrical power coefficient and the kinetic energy waste due to lower jet velocities. Furthermore, there is a reduction of the total pressure recovery due to pressure gradients inside the duct, causing high distortion. Overall, this research highlights the importance of reducing wasted kinetic energy in the combined wake and jet flow, which leads to lower propulsive power, and whose benefits can be fully exploited if newer engine technologies are provided.

Keywords: Box-Wing; Boundary layer ingestion; Wind-tunnel test; Power balance; Total pressure recovery

1. Introduction

According to the International Air Transport Association (IATA), the worldwide commercial jet fleet will double in size by 2037, and the air travel industry will be 2.5 times greater in 20 years [1]. Such growing concerns have affected the environmental policies of the aviation industry, leading to recognize the need for greener aircraft technologies [2, 3, 4]. In this context, IATA set some of the most ambitious goals, including a 1.5% annual improvement in fuel efficiency (carbon neutral growth by 2020), and a 50% decrease in CO_2 emissions by 2050, compared to 2005 levels [5]. These targets require a significant reduction in aircraft fuel-burn or the replacement of fossil fuels. Alternative and unconventional technologies, such as novel aircraft layouts, revolutionary structures and materials, and newer propulsion systems, continue to be investigated in response to these issues [6, 7].

Combining some of the aforementioned technologies, the Department of Aeronautical Engineering, at the São Carlos School of Engineering - University of São Paulo (EESC - USP) investigated potential next-generation technologies for an aircraft design to satisfy the IATA targets. That is how the INTI (Innovative Transport Industry) aircraft is presented, which combines the potential benefits of a Box-Wing (BW) design with a Boundary Layer Ingestion (BLI) propulsion system. This unconventional configuration, which has the potential to save a large amount of fuel compared to the conventional (tube-and-wing) design, is expected to provide a significant reduction of environmental impact and direct operating costs per passenger [8].

A considerable number of aircraft take advantage of the potential benefits of boundary layer ingestion to improve their performance based on a specific arrangement. For example, Blended Wing Body (BWB) with embedded engines, such as the ones presented in the NASA N+3 program [9]; aft-mounted engines on the upper surface of fuselage, such as the D8 aircraft [10], and the Airbus

Nautilius [11]; and cylindrical fuselage with circumferential aft-mounted fan, such as the STARC-ABL [12] and CENTRELINE [13] concepts. According to the findings of these investigations, BLI could be a promising method for reducing fuel consumption by offering power savings in the range of 6% to 12% compared to podded-mounted engines [14].

Different interpretations of the physics involved in BLI are represented by several methodologies. In terms of computational analyses, the most significant aspect is to represent inlet distortion concerns using propulsor models that accurately capture both flow physics and implementations, such as pressure rise, losses resulting from the fan blades and ducts, and the inlet-fan interactions for distorted inflow conditions [15]. Therefore, actuator disk methods, inlet/outlet boundary conditions, and body force models are currently being applied to evaluate the aerodynamic flow through BLI propulsors [16]. Earlier investigations of unconventional aircraft with BLI have considered one or two of these important flow simulation methods. A thorough review of previous work on numerical modeling of BLI propulsion is given by Menegozzo and Benini [17].

Conversely, when dealing with experimental analyzes, there are implementation constraints, owing to sub-scale conditions such as wall and model support interference, as well as a potentially lower Reynolds number than full-scale free flight conditions. Despite these limitations, several studies have been undertaken on this topic, using evidence from numerical simulation and wind tunnel tests to improve knowledge and provide additional insight into BLI. For example, Carter et al. [18] conducted an experimental study focused on determining the potential of highly integrated propulsion systems using BLI inlets on a BWB concept. This study determined the potential benefits of using active flow control with BLI inlets since the combination of both technologies reduces the inlet distortion and prevents flow separation which results in reduced ram and viscous drag. The results also showed a benefit up to a 10% reduction in fuel burned in comparison with pylon-mounted engines on the same configuration.

For the D8 transport aircraft, also called the "double-bubble" concept, experimental assessments indicated power savings due to BLI on the order of 6 to 8% for a zero net streamwise force, which simulates cruise condition [19, 20, 21]. These investigations focused on a back-to-back comparison using a BLI and a non-BLI concept to compare their performance. The two powered models (1:11 scale) were tested at the NASA Langley subsonic wind tunnel at speeds of 31.3 and $37.5\ m/s$, corresponding to Reynolds numbers based on model reference chord of 5.7×10^5 and 6.8×10^5, respectively. Since the power balance method was used as the theoretical framework to determine the benefit of BLI, Reynolds number impacts are minimal and low-speed results can be scaled to actual flight Reynolds numbers [22].

More recently, experimental investigations have been focused on axisymmetric fuselage concepts with an integrated BLI fan, also known as Propulsive Fuselage Concepts (PFC) [23, 24]. The geometry of the aft fuselage section of the scale model is based on the PFC configuration proposed within the CENTRELINE project. The propulsor size was scaled to reach the same ratio between the fan diameter and the fuselage momemtum thickness at the fan location, guaranteeing similarity between wind-tunnel results and full-scale aircraft. These studies characterized the flowfield around the BLI propulsor and evaluated the aerodynamic forces and moments in different flight conditions. The authors found that a PFC can generate a power saving of about 5% through an ideal BLI propulsor for an axial equilibrium condition and Reynolds number based on the wing mean chord of around 4.6×10^5.

As can be seen from literature, previous experimental studies have demonstrated the benefits of BLI, employing a large variety of geometries and electrical propulsors. The power balance method has been used as theoretical framework to evaluate those tightly integrated propulsion concepts. The primary benefit of this method is that it accounts for all power losses on the aircraft, including propulsive losses from the power plant and surface boundary layer momentum losses from the airframe [22].

Therefore, the power balance method approach was applied in this study, along with conventional thrust-drag calculations to account for the impacts of BLI using the power balance terminology.

This investigation focused on the aerodynamic behavior of the particular characteristics of the INTI aircraft using subsonic wind tunnel experiments. The analyses provide a much better understanding of the systems involved in this configuration, such as the BW layout, which reduces the induced drag, and the quantification of the BLI parameters using flow surveys at specific motor power inputs. The experimental aerodynamic measurements were conducted on a scale-model of the INTI aircraft using a non-BLI version, i.e., with nacelles assembled on pylons, and a BLI version with rear semi-buried engines. Aerodynamic forces at various angles of attack, power sweeps, wake mapping, and total pressure rake measurements demonstrated the relative contribution of each configuration to overall aircraft performance.

The outline of this paper is as follows: an overview of the INTI aircraft is described in section 2. The experimental set-up, analyses, and procedures are detailed and discussed in section 3. This section describes the wind tunnel facility, as well as the test conditions, the metrics used in the experimental procedures, and the measurement uncertainty and repeatability. Section 4 reports preliminary results at the simulated sub-scale conditions with non-BLI compared to the BLI configuration. The paper concludes with a summary of the most important findings and discussions of future works.

2. The INTI Aircraft

The INTI aircraft is a novel narrow-body jet airliner designed for investigation purposes. The INTI aircraft was designed using a low-fidelity conceptual-level Multidisciplinary Design Optimization (MDO) tool called Paerom, based on a single-point optimization strategy in which the block fuel mass is indicated as objective function. Compared to a Conventional Tube-and-Wing (CTW) concept, the INTI aircraft could reduce the fuel burn of about 12%, due to a considerable reduction in induced drag by the BW system, and the ingestion of the boundary layer developed on the fuselage [25]. It should be noted that no innovative materials or engine-core technology were explored in this study. However, additional technological advances expected to occur in the next 20 years can yield to fuel burn savings close to 30% compared to a conventional configuration with 2020 technologies.

For the present work, the most significant characteristic of the INTI aircraft is that it allows the engines to be assembled on the aft side of the fuselage, allowing them to ingest around 40% of the fuselage boundary layer. When compared to a non-BLI design, this feature allows the propulsors to use less power (about 6%) during simulated cruise condition (Mach = 0.78; Nominal Range = 1852 km; Altitude = 12500 m). Likewise, the box-wing design yields significant reductions in induced drag, providing an overall improvement in aerodynamic efficiency, while maintaining appropriate low-speed performance and static stability constraints.

The design features described above are the key characteristics of the INTI aircraft, shown in Fig. 1. The focus of this paper is primarily on BLI technology from an experimental standpoint, in order to assess the engine installation, which was designed at a conceptual level only, i.e., its benefits have only been assessed conceptually and require more investigation.

3. Experimental Set-up

3.1 Wind-Tunnel Facility

Experimental measurements were conducted in the LAE-1 wind tunnel at the São Carlos School of Engineering - University of São Paulo (EESC-USP). The test section has a rectangular cross-section of 3.0 m length, 1.3 m height and 1.7 m width. The wind tunnel has an eight-blade fan that is powered by a 110 HP electric motor and can provide speeds of up to 40 m/s in the test section. A recent update for aeroacoustic measurements decreased the turbulence levels from the original 0.25% to 0.21%. More information about the wind tunnel is reported in [26, 27, 28]. Figure 2 shows a schematic of the model inside the tunnel. It is coupled to a pitch-strut system near the fore wing's quarter chord,
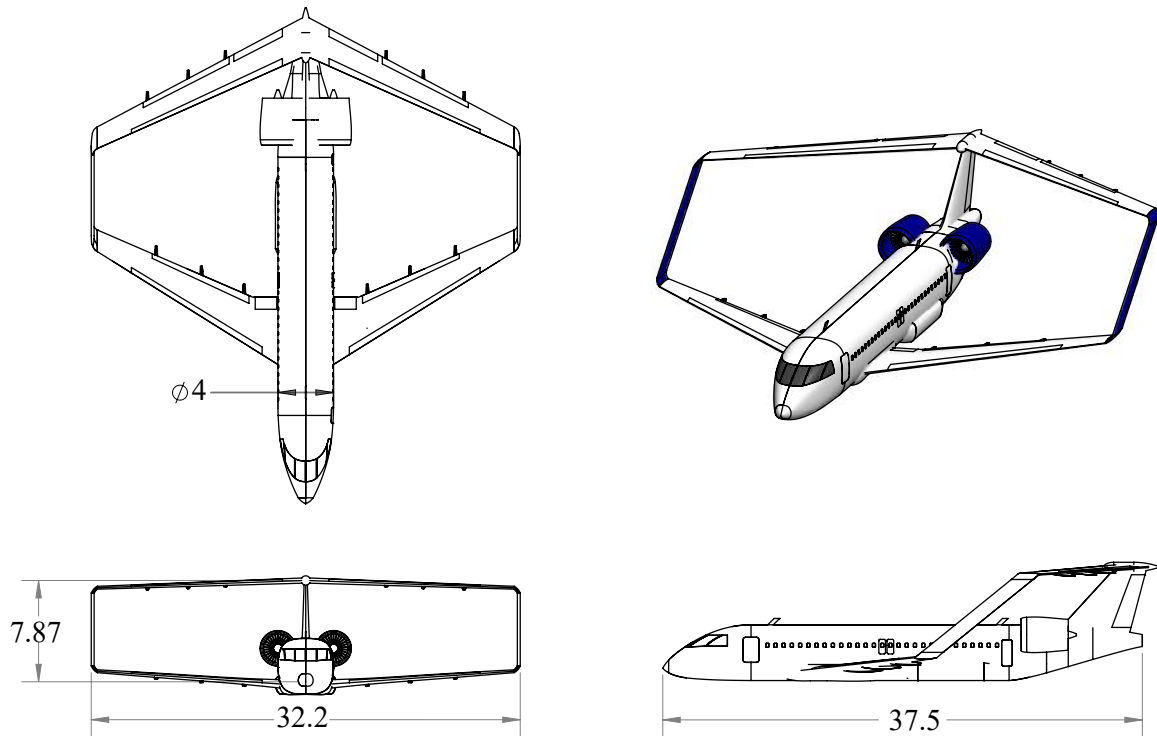
Figure 1 – General view of INTI aircraft (box-wing / BLI concept), dimensions in meters.

which controls both angle of attack and model height. The system is basically composed by a strut, a threaded bar ($NC4 - 32$), and a step motor ($KTC - 5034 - 349 - K$). The pitch-strut system was calibrated by verifying the relation between the number of steps taken by the motor and the angle of attack of the model. The step motor provides a static torque of $1.86\ N.m$, step in angle of $1.8°$ with a precision of 5%, and continuous power of $25\ W$. The model is positioned vertically so that while the angle of attack changes, a reference point at the fore wing root remains in the center of the tunnel. The uncertainty on model position within the test section (Y and Z directions) is $\pm 1\ cm$.

Note that at zero angle of attack, the 1:28 scale INTI model results in a wind-tunnel blockage of approximately 2.39%. The interaction effects between the boundary layer of the wind-tunnel walls and the model were corrected by using Computational Fluid Dynamics (CFD) simulations. In particular, the corrections were applied to relate a confined flow field to an equivalent free stream flow field, so two Reynolds Averaged Navier-Stokes (RANS) simulations were run: one in the tunnel and one in free air, both using a no-slip boundary condition on the walls of the computational domains [29]. Such an approach allowed to correct the wake blockage and angle of attack due to walls interference.

3.2 Tested Configurations

A scale model (1:28) of the INTI aircraft was designed for investigating the aerodynamic benefits of boundary layer ingestion. Three models were needed for the wind-tunnel tests: (*i*) an unpowered configuration, which was used to measure the main aerodynamic characteristics of the airframe. The schematic in Fig. 3a illustrates the main model dimensions and the conventional tail used by the non-BLI and BLI configurations with no pylons nor propulsors. Technical views and details of the electric fan used in the wind tunnel campaign are shown in Fig. 3b. (*ii*) the non-BLI configuration, shown in Fig. 4a, which has podded engines with axisymmetric nacelles that are assembled on pylons at the rear part of the aircraft for ingesting clean airflow. (*iii*) The BLI configuration, shown in Fig. 4b, which is designed with rear semi-buried engines in order to capture a relatively large part of the boundary layer developed over the fuselage.

The airfoils of the BW model differ from the full-scale configuration due to the subsonic nature of
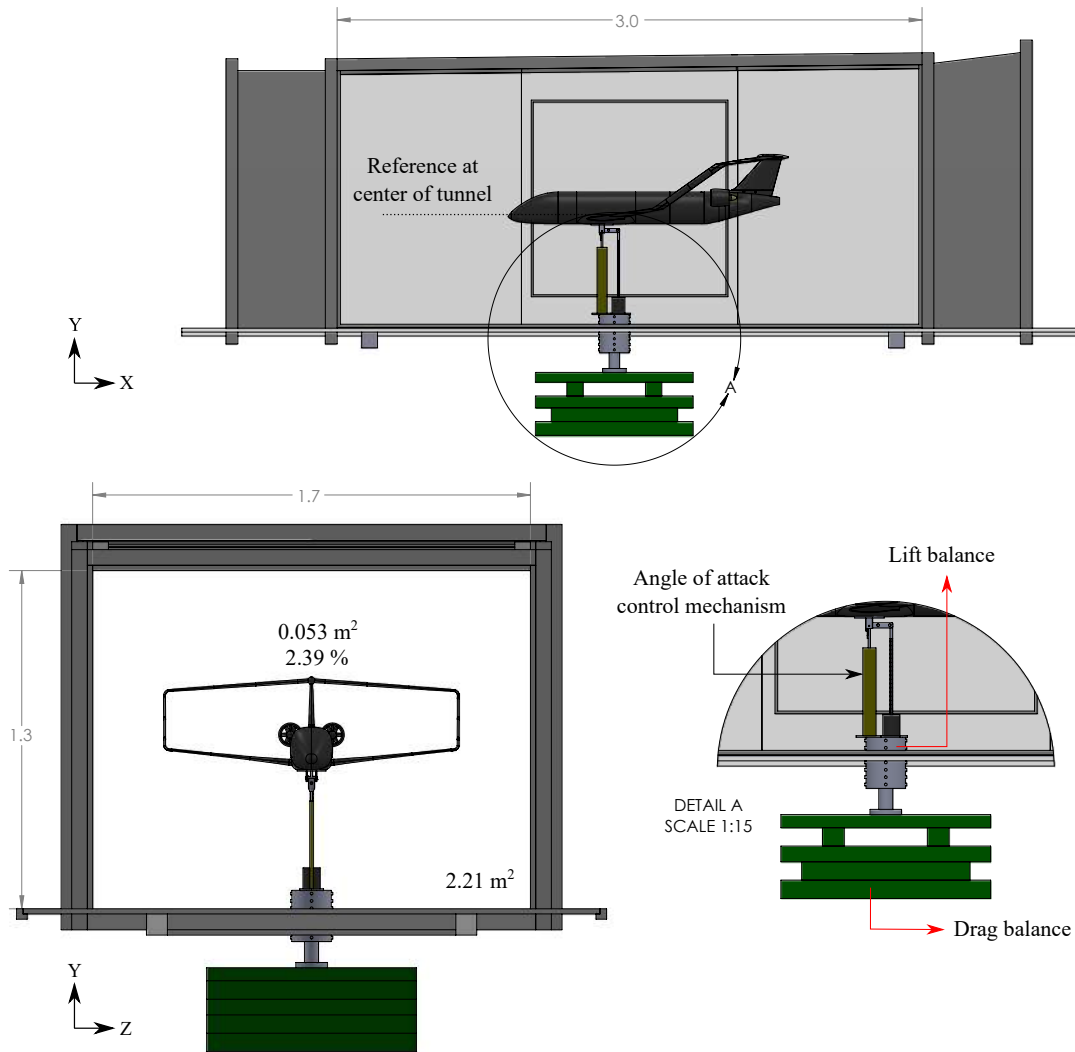
Figure 2 – Schematic views (side and front) of the INTI model in the test section of LAE-1 wind tunnel, dimensions in meters.

wind-tunnel tests. This is important to provide adequate behavior at relatively low test Reynolds numbers. In this context, two methods were used to find a match between experimental and full-scale aircraft performance. The first was to ensure lift coefficient equivalency by employing proper airfoils, and the second was to force boundary layer transition by using trip strips on all model surfaces (wings, fuselage, tail, and propulsor nacelles). The thickness and position of the trip strips were established by ensuring that the drag coefficient increased uniformly as tunnel speed decreased, as recommended by Barlow, Rae, and Pope [30]. This method ensured the presence of fully turbulent boundary layers on the model at some representative condition. A 3 mm wide and 0.08 mm thick strip (grit size) was placed over the complete aircraft model. For the closed-wing system, trip strips were located at $x/c = 0.05$ on its suction side, and on its pressure side at $x/c = 0.10$. For fuselage and nacelles, the trip strips were located at 5-10% of the body length. This ensures the development of fully turbulent boundary layers during the experimental campaign.

The models were created using additive manufacturing techniques. A total of 48 pieces conformed the mockups, and carbon fiber beams reinforced the closed-wing structure. The pieces were assembled manually, meeting manufacturing tolerances based on the Computer-Aided Design (CAD) process. The aerodynamic surfaces were then treated and painted for ensuring a smooth surface finish. Note that the non-BLI, BLI, and unpowered models share the same physical components, except for the removable tail cone. The connections between these components were adjustable,

Lateral view

Top view

(a) Technical views of the wind-tunnel unpowered model.

(b) Detail drawings of the EDF for powered configurations.
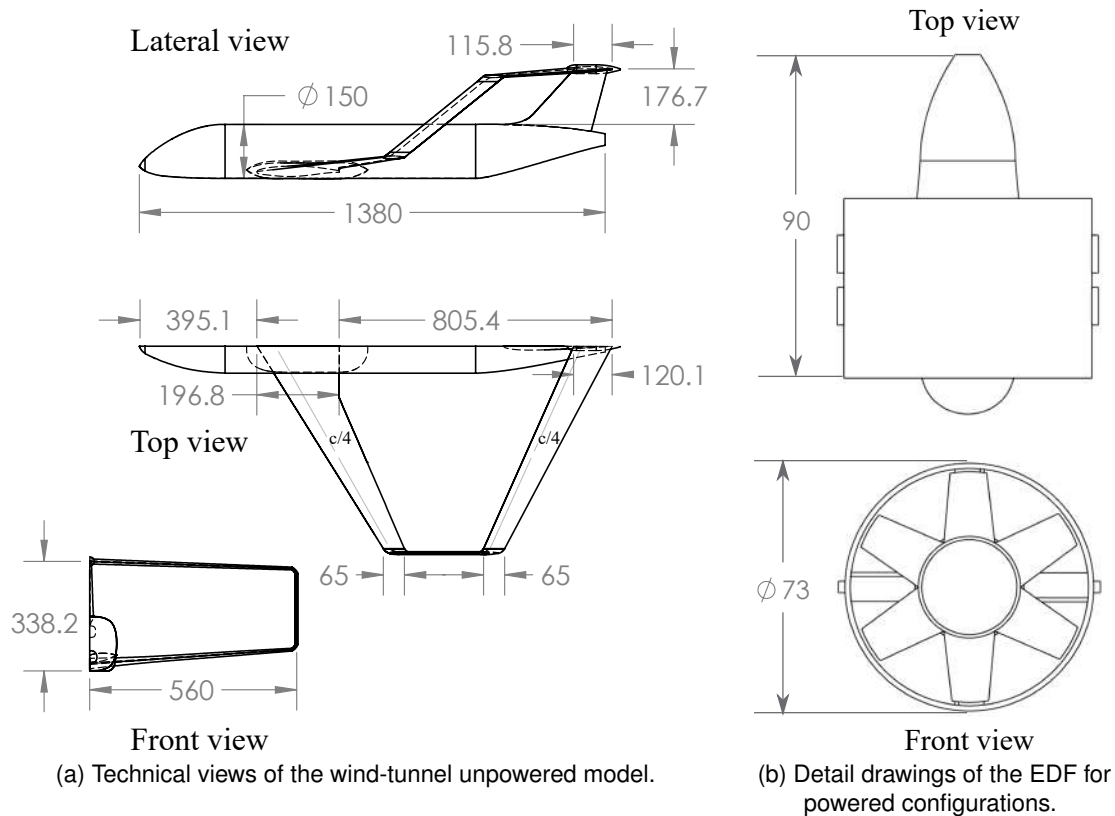
Figure 3 – Details of the unpowered model and electric fan equipping the wind-tunnel powered models, dimensions in millimeters.

with the parts clamped together with set screws.

The model instrumentation includes 13 static pressure taps distributed inside the duct of the BLI configuration. Both non-BLI and BLI models are powered by two QF2827-2300KV Brushless Motors (6 blades), a commercial Electric Ducted Fan (EDF), typically used for R/C models. The central duct has an outer diameter of 70 mm and total length of 58 mm. The fan's nominal voltage is 8 - 22 VDC and the maximum electrical current allowed is 50 A. The maximum thrust of each fan is 16.77 N at 30000 RPM. The EDFs were controlled by a Readytosky 50A (ESC) and powered by a RSP-3000-48 power supply. The motor shaft rotational speed was determined using an optical tachometer that uses a laser light to accurately measure the speed in RPM. The speed controllers were located inside the fuselage of the model, requiring about 5 meters of wire length between the ESC and the power supply. Finally, the propulsor power was varied by setting the fan wheel speed using a SIKAF RC Servo speed controller. Some important values of the scaled models are presented in Table 1.

Table 1 – Reference dimensions of the 1:28 INTI models.

Dimension	Value
Reference area $[m^2]$	0.25
Reference chord $[mm]$	160
Wingspan $[mm]$	1120
Length $[mm]$	1380
Inner diameter of fan $[mm]$	73

3.3 Test Conditions

The LAE-1 wind tunnel was operated at velocities of about 27 m/s and 30 m/s, which correspond to Reynolds numbers based on the reference chord length of 2.72×10^5 and 3.02×10^5, respectively.

(a) Non-BLI model configuration.

(b) BLI model configuration.
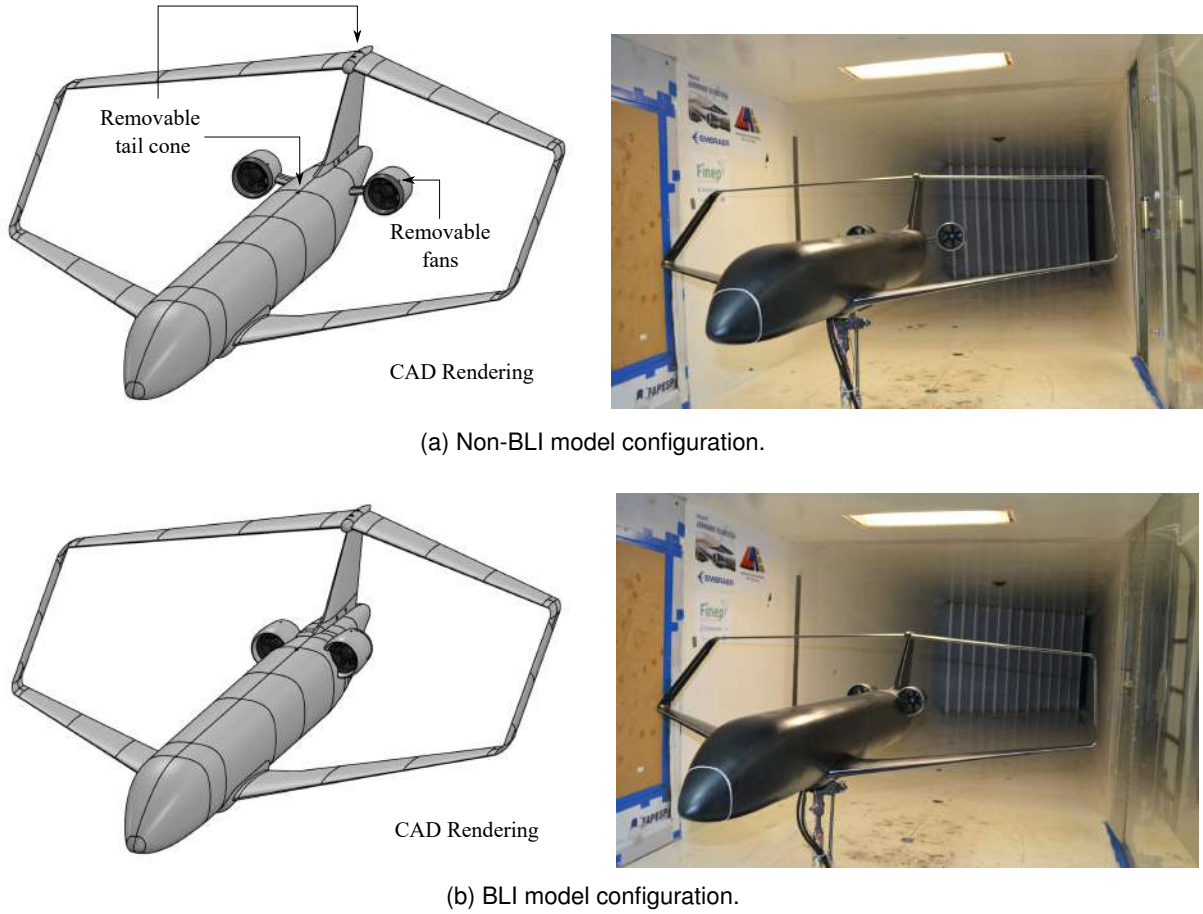
Figure 4 – INTI models: CAD rendering of mockups, and photographs of the wind-tunnel setup assembled in the test section of the LAE-1 subsonic wind tunnel (scale 1:28).

These velocities were carefully determined after testing the propulsor thermal and model structural capabilities. The latter was generally the limiting constraint. At the beginning of each test, atmospheric conditions were monitored in order to establish non-dimensional parameters. A calibrated mercury barometer with a 1 $mmHg$ precision measured the atmospheric pressure. A thermocouple measured the temperature inside the wind tunnel. Relative humidity was measured by a hygrometer and was then used to determine the air density. Dynamic pressure was measured by a pitot-static probe located at the test section, which is connected to a micro-manometer (TSI Model 8705 DEP-CALC; uncertainty of $\pm$ 0.1 Pa). The model was installed on the pitch-strut system and remained there until the test campaign was completed. Changes of the tail cone and instrumentation of the fans were undertaken insitu. The reference quantities of the tunnel operating conditions are listed in Table 2, whereas the propulsor non-dimensional fan wheel speeds implemented during the tests are given in Table 3.

The ratio between the fan blade tip speed and the tunnel speed (U_{tip}/V_∞) is used to assess the effect of the propulsors on the flow features, where the fan blade tip speed is defined by Eq. 1:

$$U_{tip} = \Omega_f \frac{d_{fan}}{2} \qquad (1)$$

where Ω_f is the fan wheel speed, and d_{fan} is the model propulsor fan diameter, equal to 73 mm.

3.4 Data collection

Four main types of runs were performed:

1. Force measurements (Lift and Drag) were taken for the unpowered, non-BLI, and BLI configurations, in order to quantify their aerodynamic behavior at several angles of attack (α). In this

Table 2 – Non-dimensional flow parameters for different tests.

Freestream velocity [m/s]	Dynamic pressure [Pa]	Mach number [-]	Reynolds number [-]
27.0	410.9	0.080	2.72×10^5
30.0	507.3	0.089	3.02×10^5

Table 3 – Propulsor dimensional and non-dimensional wheel speeds

Ω [RPM]		9000	10300	15500	18200	20400
U_{tip}/V_∞ [-] at	$V_\infty \approx 27.0\,m/s$	1.33	1.44	2.17	2.55	2.86
	$V_\infty \approx 30.0\,m/s$	1.20	1.30	1.96	2.30	2.58

case, the engines were easily disassembled from the nacelle to obtain through-flow nacelle conditions. This approach allowed for the analysis of pure geometry effects. To provide some form of experimental validation, the wind tunnel results for the unpowered configuration were compared to CFD simulations. The angles of attack measured ranged from $\alpha = -4°$ to $12°$ in $1°$ steps.

2. Electrical power (P_E) measurements were performed for the powered configurations, i.e., with the engines assembled on the non-BLI and BLI models. The objective of this experiment was to determine the electrical power coefficient, along with the net streamwise force (F_X) for a range of fan wheel speeds, fixed angle of attack, and fixed tunnel velocity. A set of fan wheel speeds were defined, and force and power readings were recorded. The product between the voltage input to the ESC (v) and the current from the power supply (i) determined the electrical power supplied to propulsors ($P_E = vi$).

3. Flow field measurements were conducted for both powered and unpowered models. The goal here was to determine the variation of axial flow velocity (u^*) between configurations in a transversal plane; therefore, aerodynamic measurements are presented by considering the streamwise velocity contours, and flow mapping for selected fan wheel speeds, fixed angle of attack, and fixed tunnel velocity. In particular, for powered configurations, the flow surveys were conducted at power levels that bracket zero net streamwise force.

4. Inlet pressure distortion measurements were carried out on the models with the fan uninstalled, in order to evaluate the dependence of the distortion on the INTI airframe at various points in the flight envelop, and to establish differences in the distortion level between a non-BLI and a BLI configuration. In this case, total pressure rake surveys were conducted at fixed tunnel velocity, and angles of attack ranged from $0° < \alpha < 8°$ in $1°$ steps.

Finally, polyester mini-tuft flow visualization is used to assess the flow on the aerodynamic surfaces of the models at specific flow conditions.

3.5 Measurement techniques

3.5.1 Aerodynamic forces

The aerodynamic forces acting on the models were measured by a two component balance, as illustrated in detail A of Fig. 2. The drag balance was built in the Laboratory of Experimental Aerodynamics at EESC-USP. Conversely, a second balance measured the lift force which is composed by two strain gauges placed on flexures stiffeners forming a Wheatstone bridge. More details of the lift balance and angle of attack control mechanism can be found in [31], whereas previous aerodynamic results using the current balance scheme can be found in [32, 33]. The signals are recorded by a data NI AT-M10-16X acquisition sheet of 500 Hz sample frequency. Prior to the experiments, the aerodynamic balances were calibrated by loading known weights in order to create a linear voltage-force ratio. The complete scheme has, at maximum loading, measurement accuracy of +0.7%; therefore, for lift, drag, and angle of attack, the accuracies are $\pm 0.8\,N$, $\pm 0.18\,N$, and $0.2°$, respectively.

The net streamwise force can be defined as the difference between the drag and thrust [19], being positive in downstream direction. In its non-dimensional form, the net streamwise force coefficient (C_X) is expressed by:

$$C_X = \frac{T_{EDF} - D}{q_\infty S} = C_T - C_D \tag{2}$$

where T_{EDF} is the thrust generated by the EDFs, D is the drag of the model, q_∞ is the freestream (tunnel) dynamic pressure, S is the wing reference area, C_T is the thrust coefficient, and C_D is the drag coefficient. In this case, the experiment was carried out in search of a zero net streamwise force, which is calculated using the load cell of the drag balance, measuring the difference between the propulsor's gross thrust and the model's drag. The pitch-strut system drag was subtracted from the model's drag to determine the main aerodynamic characteristics of the aircraft. This process involved a simple approach to evaluate the tare (direct drag of the support), in which the forces on the pitch-strut system (i.e, removing the model) are measured at different tunnel speeds, and the drag generated by the support is corrected in function of the tunnel dynamic pressure using regression statistical analysis [30].

To determine the primary aerodynamic coefficients, the wind tunnel data of the unpowered configuration is compared to CFD simulations. In this case, the geometry of the model was discretized using **ANSYS** meshing. The atmospheric conditions of the experimental setup were adjusted to the computational setup. Two computational domains with different sizes were considered: a small one to simulate the confined flow of the wind tunnel, and a large one to simulate free air conditions. The drag difference between these simulations was subtracted to the drag of the wind tunnel model to account for wall effects. An unstructured tetrahedral mesh was used in all the simulations, as shown in Fig 5a. Grid density is regulated near the aerodynamic surfaces to increase the grid's resolution in that region. The dimension of the cells in the refinement area is limited to $0.02\ m$. The surface meshes were influenced by structured cells (prism) in order to capture the boundary layer effects with adequate precision. The near wall treatment was adjusted in terms of the total thickness, with 20 sub-layers and a growth rate of 1.2. The boundary layer refinement kept the dimensionless wall distance value (y+) close to 1.0. The Figs. 5b and 5c show close-up views on the surface meshes. The generated mesh of the large domain features a total of 6.32 million nodes.

The inlet velocity is set to 30 m/s whereas turbulent intensity is set to 0.21% based on wind tunnel turbulence level [27]. On the symmetry plane of the domains, symmetric boundary condition is applied, while the model surfaces are treated as no-slip walls. The outlet surface of the domains is modeled as a pressure outlet. Steady simulations using the SST turbulence model are carried out for the CFD validation. Second-order schemes are used for all the flow, i.e., the advection terms and turbulence numeric were discretized using a high resolution scheme. The convergence control was set to reach 600 iterations, with a residual target equal to 1×10^{-5}.

3.5.2 Application of the power balance equation

The main equation of the power balance method is derived in this section. The power balance method is a solution presented by Drela [22] to evaluate the performance of highly coupled systems. Basically, this method focuses on a mechanical power and kinetic energy analysis, instead of focusing on momentum equation analysis. For a control volume which fully envelopes the propulsor, and assuming a low speed, the only input power term in the power balance equation is the mechanical flow power (P_K), which is calculated by:

$$P_K \equiv \oiint (p_{t\infty} - p_t)\, \mathbf{V} \cdot \hat{n}\, d\mathscr{S} \tag{3}$$

where p_t and $\mathbf{V}$ represent the flow stagnation pressure and the local velocity vector, respectively, $\hat{n}$ is the normal vector which points into the propulsor, and $d\mathscr{S}$ is the surface differential. According to Uranga et al. [19], the mechanical flow power can be measured with two different methods,
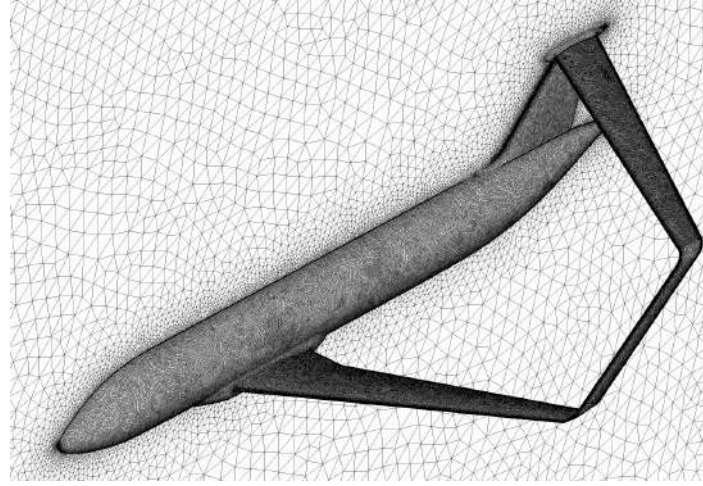
(a) Mesh global view.
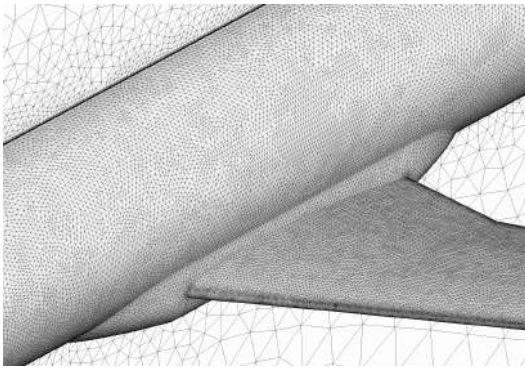
(b) Close-up view for wing-fuselage intersection.
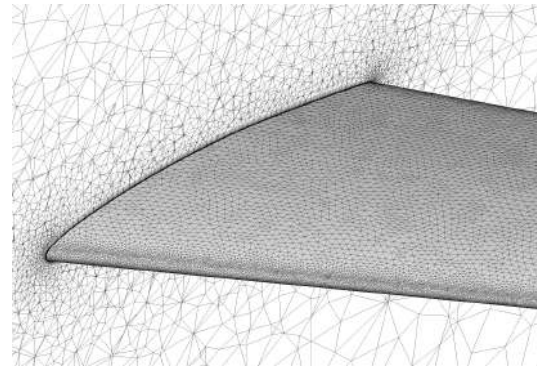
(c) Close-up view of boundary layer prism on wing.

Figure 5 – Mesh structure for unpowered configuration.

i.e., the direct and indirect method. The direct method consists of surveying the propulsor inflow and outflow planes with flow measurement techniques (e.g., PIV, 5-hole probe, or rotating P_t-rake system). The indirect method, on the other hand, determines the mechanical flow power from the measured electrical power supplied to the motor, combined with the fan efficiency (η_f) and motor efficiency (η_m). Such quantities can be non-dimensionalized as follow:

$$C_{P_K} \equiv \frac{P_K}{q_\infty V_\infty S} \tag{4}$$

$$C_{P_E} \equiv \frac{P_E}{q_\infty V_\infty S} \tag{5}$$

$$C_{P_K} = \eta_f \eta_m C_{P_E} \tag{6}$$

The BLI benefit is given by the Power Saving Coefficient (PSC), where the objective is to obtain the required power to achieve a zero net-streamwise force:

$$PSC \equiv \frac{(C_{P_K})_{non-BLI} - (C_{P_K})_{BLI}}{(C_{P_K})_{non-BLI}} \tag{7}$$

In these experiments, it was assumed that the fan and motor efficiencies do not differ considerably between the BLI and non-BLI configurations for the same operating point. Indeed, initial motor characterization indicated the motor operates close to its maximum efficiency, i.e., > 71% (data from EDF's data sheet). Such an approach is considered a surrogate to evaluate the flow power, since the electrical power can be directly measured during the wind tunnel tests [34]. Therefore, it is assumed that the BLI benefit can be computed as:
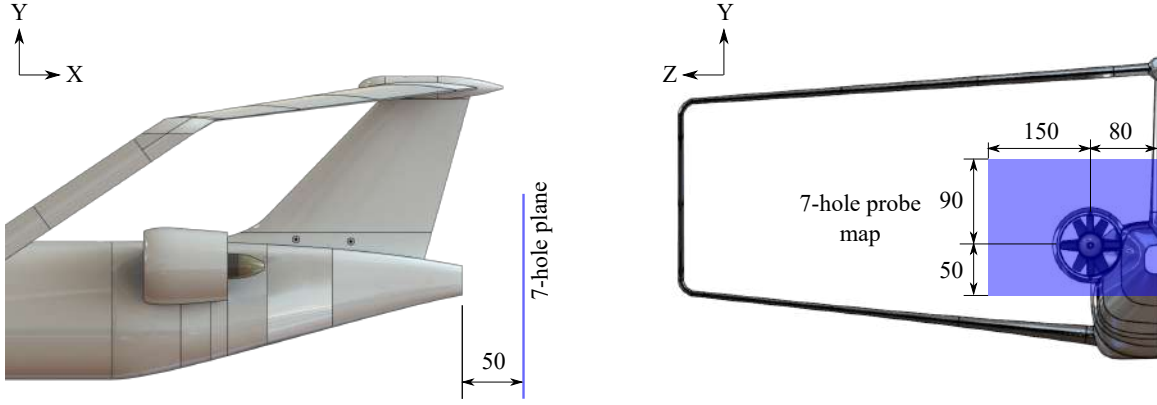
Figure 6 – Grid dimensions for wake mapping with 7-Hole Pitot probe, dimensions in millimeters.

$$PSC \equiv \frac{(C_{P_E})_{non-BLI} - (C_{P_E})_{BLI}}{(C_{P_E})_{non-BLI}} \tag{8}$$

Note that the assumption of maintaining constant efficiencies for the BLI benefit leads to higher uncertainty. In this case, the uncertainty in the BLI benefit is found to be $\pm 2.5\%$.

3.5.3 Flow mapping
Flow-field measurements were performed using a L-shape 7-hole probe (AeroProbe® system). It is composed by a conventional cylindrical body (stainless steel 3.2 mm diameter) with seven holes at its tip. The probe is adequate for wind tunnel testing since its tip is directly in the airflow, and the probe is attached to the side so that the data obtained is not disrupted. The probe allows for highly accurate measurements of flow vector magnitude and direction, as well as static and total pressure. The acceptance angle is up to $\pm 30°$ with an error rate lower than $\pm 1°$. The velocity error is lower than $\pm 1\%$ and can have up to 500 discrete aerodynamic calibration points per speed [35]. The calibration of the 7-hole probe was done using a neural network trained with input data from $\pm 30°$, 1-degree precision in Y and Z direction, and RMS-error of 0.1 m/s.

A three-axis traverse system (DANTEC® traverse system) was used to move the sensors in a specified grid for obtaining the wake characteristics. The system moved the probe in three directions at micrometer accuracy. In particular, each axis movement has 0.0125 mm accuracy, and was operated by serial communication. The traverse system was fixed at approximately 50 mm away from the fuselage tail cone, where a rectangular transversal plane was used to measure the flow pattern of the propulsor jet. With the center of the fan diameter as a reference, the grid of the rectangular transversal plane was set from 150 mm to -80 mm with a 5 mm spacing in the lateral direction, and from -50 mm to 90 mm with a 5 mm spacing in the vertical direction. The data average was calculated using 500 samples from 5 seg measurements. The probe was traversed through the same grid points in space, and time-averaged values for all three velocity components (u^*, v^*, w^*) and velocity fluctuations (u_{rms}, v_{rms}, w_{rms}) are obtained at each point. Thus, the in-plane velocity vectors (v^* and w^*) are used to calculate streamwise vorticity (ω_x). The dimensions of the grid planes for the wake mapping are shown in Fig. 6, whereas the complete wake mapping experiment, mounted on the wind tunnel test section is shown in Fig. 7.

3.5.4 Steady total pressure distribution and distortion analysis
The inlet efficiency was evaluated through the total pressure coefficient (Eq. 9) and the distortion index (Eq. 10), as follow:

$$C_{p_t} = \frac{p_t - p_{t_\infty}}{q_\infty} \tag{9}$$

$$DC_\theta = \frac{p_{t_{AIP}} - p_\theta}{q_{AIP}} \tag{10}$$

11
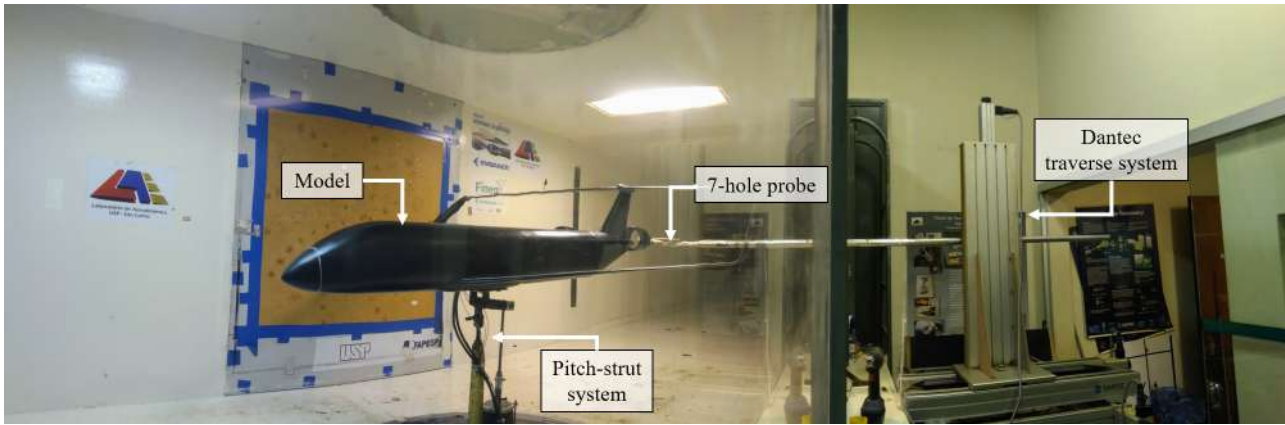
Figure 7 – Overview of the wake mapping experiment in the test-section.
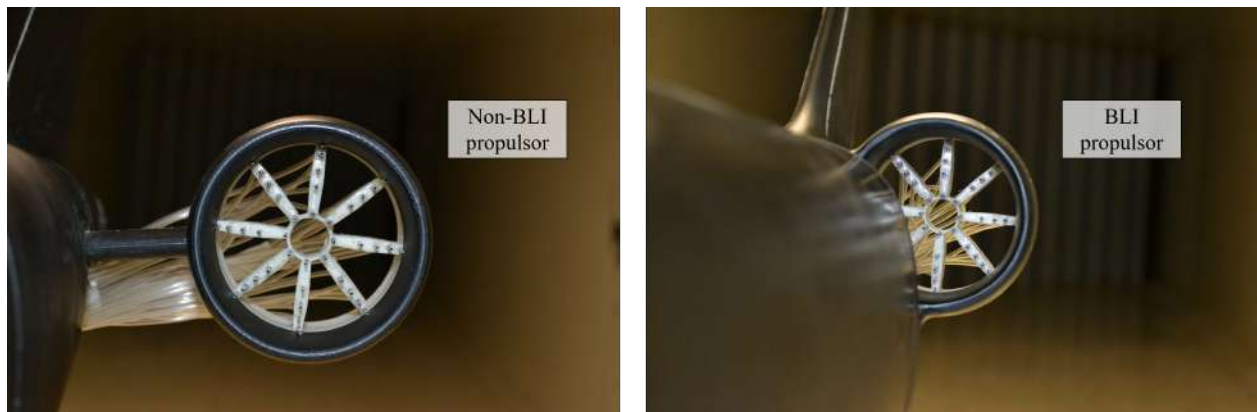
Figure 8 – Total pressure rakes installed on the wind-tunnel models.

where $p_{t_{AIP}}$ is the average total pressure value in the survey plane ($360°$), p_θ is the minimum average total pressure value in a sector of $60°$, and q_{AIP} is the mean dynamic pressure calculated by $q_{AIP} = \rho V_{AIP}^2/2$. The goal of these tests was to look inside the engine inlet duct and study if there is a significant difference in overall pressure across the Aerodynamic Interface Plane (AIP) between the configurations. The total pressure distribution at the AIP was measured with a total pressure rake with an outer diameter of 70.5 mm. The rake was located in a plane perpendicular to the freestream velocity direction, as shown in Fig. 8.

The rake is characterized by 40 total pressure probes, distributed in 8 circumferential locations with $25°$ of circumferential spacing, and 5 radial locations. For each configuration and condition, the pressure data were recorded through a pressure scanner (Scanivalve® DS4-48) for a period of 5 seg and averaged over this period (the pressure rating is 0.01 to 100 psi). The Scanivalve has an electro-mechanical pressure multiplexer which allows to read and transmit several input signals sequentially thanks to a solenoid. The position transmitter (encoder) electrically indicates the port being measured, and a solenoid stepper drive provides sequential connection of ports to 48 transducers. The signal conditioner gain was set to the full scale pressure range of the transducer, i.e., for 5 V ($20mA$) output [36]. The freestream static and total pressures were measured simultaneously with a Pitot static probe positioned at the test section's inlet and acquired using the same pressure scanner. In this way, possible changes in the freestream conditions owing to temperature or velocity drifts were accounted for. The uncertainty of the measure was 1% for each type of run.

3.6 Measurement Uncertainty

All measurements are susceptible to some degree of uncertainty. Therefore, measurements were carried out with extreme caution in order to avoid random and systematic errors that arise in any experimental measurement situation. In this study, several types of experimental uncertainties were

examined, along with some methods of error and data analysis that can be used in subsequent experiments. The uncertainty in tunnel operating conditions was obtained from the precision of the tunnel instrumentation. This way, the same magnitude and sign of experimental uncertainty are obtained when the measurement is repeated several times.

The uncertainty of BLI measurements depended on the electrical power uncertainty and measured net streamwise force. The instrument precision of electrical power was calculated by error propagation of voltage and current, with the 1.1% precision error in the monitor of the power supply. These instrumentation uncertainties were propagated to the quantities of interest, assuming that all uncertainties are statistically independent [30], as follows:

$$\delta R = \left[\left(\frac{\partial R}{\partial x_1} \delta x_1 \right)^2 + \left(\frac{\partial R}{\partial x_2} \delta x_2 \right)^2 + \left(\frac{\partial R}{\partial x_3} \delta x_3 \right)^2 + ... + \left(\frac{\partial R}{\partial x_n} \delta x_n \right)^2 \right]^{\frac{1}{2}} \quad (11)$$

where R is a function of N independent variables $(x_1, x_2, ..., x_n)$. In executing Eq. 11, each term is calculated with only one variable augmented by its uncertainty interval, all others being at their recorded values.

Finally, uncertainty of distortion measurements depended on scanivalve pressure sensors and disposition of each probe in the total pressure rake. In this case, the readings from the scanivale provided the differential pressure of each probe in relation to the central total pressure probe, which was used to determine the standard deviation of reading. Thus, the values of the deviation from the average value were used to calculate the experimental error. The possible errors in each measurement were assumed normally distributed; so the error in each measurement was assumed independent of the error in any other measurement, and the error in every measurement was described at the same confidence level.

3.7 Repeatability

Repeatability refers to the agreement among repeated measurements, i.e., the spread of the collected data or how close they are together. The more precise a set of measurements, the closer together they are. In this study, several data sets pertaining to determined experiment were repeated in order to assess the repeatability of the wind-tunnel observations. In particular, aerodynamic measurements were repeated five times per tunnel velocity and range of angle of attack; electrical power measurements were repeated seven times per tunnel velocity and angular velocity of EDFs; flow mapping measurements were repeated two times per angular velocity of EDFs; and inlet pressure distortion measurements were repeated three times per tunnel velocity and range of angle of attack. The deviations of the measurements with respect to the mean value are computed per data set. These deviations were used to evaluate the confidence intervals using a Student's t-distribution. The data collected during a given run is fitted with a polynomial curve, indicating 95% of confidence intervals. Despite the fact that some angles of attack have a broader range of variation, the experiment is considered repeatable.

4. Results

4.1 Aerodynamic measurements

In this section, the experimental and CFD results for the unpowered configuration are first analyzed and compared (Fig. 9). Alpha sweeps (from $\alpha = -4°$ to $12°$ in $4°$ steps) using the converged grid were run to better understand the offset from experimental data. Experimental force measurements results of the three configurations in through-flow nacelle condition are also presented and discussed (Fig. 10). Lift and drag coefficients, drag polar, and aerodynamic efficiency are the variables evaluated. Table 4 shows a summary of the results from the experimental-numerical comparison of the unpowered configuration, as well as differences between the experimental curves of the configurations.

Figure 9a shows the comparison of lift coefficient in function of angle of attack. The lift curves show correlation for low to moderate angles of attack between the two methods, since the curves display a linear behavior with a similar slope ($\partial C_L / \partial \alpha$) from $\alpha = 0°$ to $5°$ (See Table 4). However, the CFD

Table 4 – Aerodynamic forces of the configurations in through-flow nacelle condition at $M = 0.089$ and $Re = 3.02 \times 10^5$.

Configuration	Unpowered			Non-BLI		BLI	
Parameter	Exp	CFD	% error	Exp	Δ [%]	Exp	Δ [%]
C_L for zero α [-]	0.181 ± 0.0084	0.191	5.52	0.187 ± 0.0093	3.31 ± 0.11	0.184 ± 0.0097	1.65 ± 0.15
$\partial C_L / \partial \alpha$ [-]	0.102 ± 0.0118	0.111	8.82	0.102 ± 0.0106	0.0	0.102 ± 0.0113	0.0
C_{Lmax} [-]	$0.985_{|11°} \pm 0.0157$	$1.092_{|12°}$	10.86	$0.997_{|10°} \pm 0.0138$	1.21 ± 0.12	$1.004_{|10°} \pm 0.0149$	1.92 ± 0.10
C_D for zero α [-]	0.0304 ± 0.0042	0.0245	19.40	0.0338 ± 0.0064	11.18 ± 0.52	0.0319 ± 0.0051	4.93 ± 0.21
$\partial C_D / \partial C_L^2$ [-]	0.0217 ± 0.0107	0.018	14.28	0.0226 ± 0.0101	4.14 ± 0.05	0.0224 ± 0.0099	3.03 ± 0.07
$(L/D)_{max}$ [-]	$17.21_{|6°} \pm 0.0098$	$22.05_{|6°}$	28.12	$15.77_{|6°} \pm 0.0010$	8.36 ± 0.89	$16.67_{|6°} \pm 0.0088$	3.13 ± 0.10

(a) Lift Coefficient.

(b) Drag polar.
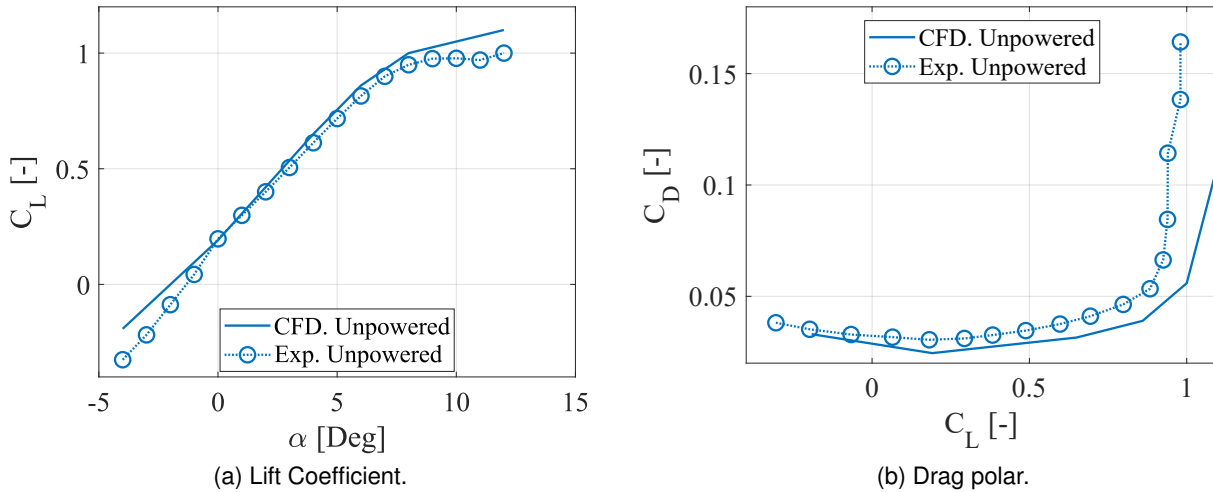
Figure 9 – Alpha sweep of CFD and experimental results for unpowered configuration at $M = 0.089$ and $Re = 3.02 \times 10^5$. Repeatability is $\Delta C_L = 0.007$ and $\Delta C_D = 0.003$.

results over predict lift at negative angles. This could be explained by the fact that the wind tunnel models had strips on both sides of wing section, artificially increasing the boundary-layer thickness and reducing the model's effective curvature. Note that a greater dispersion (on the order of 11%) at high angles of attack is found due to the higher level of complexity in the flow pattern arising from the stall region, which is more difficult to be numerically simulated. Despite the $C_L - \alpha$ curve matched well among all the simulations, there is an offset from the experimental data by approximately $-0.3°$ in angle of attack. This can be seen in Table 4 where the C_L for zero α has an error of 5.52%, which is explained by the calculated uncertainty of the pitch-strut system, i.e., the effective angle of attack of the wind-tunnel model might have been higher than the geometric angle of attack. At this point, additional investigations are needed to determine the reason of the shift.

Figure 9b depicts the complete drag polar chart for the unpowered configuration. The CFD results show under predictions with the experimental data in all evaluated angles of attack, where the values at zero angle of attack were 0.0245 and 0.0304, respectively (error rate of 19.4%). Although there is an offset in drag levels between the fully turbulent computation and the experimental data, the curves show relatively good agreement at low to moderate angles of attack. It should be noted that increasing grid density will result in a better approximation of numerical data in terms of C_D. On the other hand, the experimental curve showed larger drag values as the angle of attack increased. The reason of that difference is due to vibrations of the model under the effect of stall detachments, increasing the predicted drag values.

The experimental results of the unpowered configuration, as well as non-BLI and BLI configurations in through-flow nacelle condition are presented in Fig. 10. According to the lift coefficient results (Fig. 10a), the nacelle induces a gradually increasing amount of extra lift between $\alpha = 0°$ and $\alpha = 5°$;

(a) Lift Coefficient.

(b) Drag Coefficient.

(c) Drag polar.

(d) Lift-to-Drag ratio.
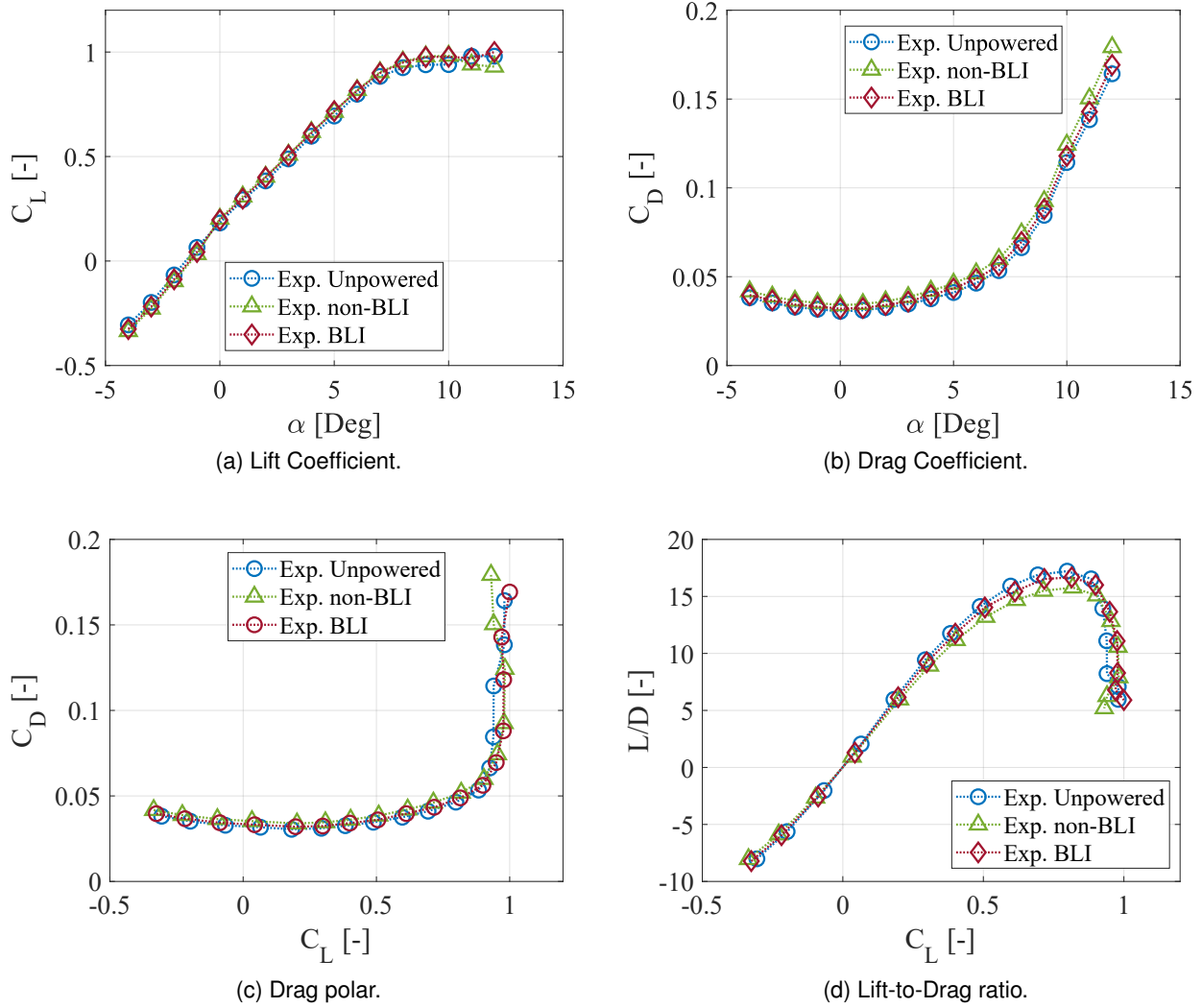
Figure 10 – Alpha sweep of wind tunnel configurations in through-flow nacelle condition at $M = 0.089$ and $Re = 3.02 \times 10^5$ comparing free-air lift and drag with corrected experimental data. Repeatability is $\Delta C_L = 0.007,\ 0.009,\ 0.007$ for unpowered, non-BLI, and BLI configurations, respectively. Repeatability is $\Delta C_D = 0.003,\ 0.004,\ 0.004$ for unpowered, non-BLI, and BLI configurations, respectively.

however, the change in lift is relatively small. At high angles of attack (i.e. from $\alpha = 8°$ to $\alpha = 12°$), the configurations exhibited a smooth stall behavior, which can be explained by the mutual interaction of the wings, in which the aft wing continues to provide lift, while the fore wing has already started the stall process. As a result, in the poststall regime, the lift coefficient does not drop rapidly, resulting in a nose pitch-down tendency. Such characteristic allows BW concepts to avoid risks due to stall effect when approaching stall angle, maximizing the total lift without creating adverse trim effects. This has a significant impact on safety, especially in commercial aircraft categories. This behavior was also observed in the IDINTOS project, where low-speed wind tunnel results showed the mutual interference between the wings, which changed at different angles of attack [37]. The mini-tuft flow visualization technique applied on the main box-wing surfaces near stall conditions also confirmed this behavior (Fig. 11). The mini-tufts indicated a region of blurred tufts flow on the fore wing, whereas the flow on the aft wing was completely unseparated.

The impact of through-flow nacelles on the overall aircraft drag was also evidenced by comparing the experimental curves (Fig. 10b). As expected, the non-BLI configuration showed an increase in total drag due to the contribution of pylons, as well as the contribution of nacelle drag. The mutual aerodynamic interference between the pylon and the nacelle increased drag of about 11% in comparison

Figure 11 – Mini-tuft flow visualization on the wing surfaces at $M = 0.089$, $Re = 3.02 \times 10^5$, and $\alpha = 10°$.

with the unpowered configuration. In contrast, the BLI configuration increased drag on the order of 5% compared to the unpowered configuration, indicating that the magnitude of interference drag of the BLI model is lower than the non-BLI model, i.e., the BLI model allows for smaller nacelles and eliminates pylons, reducing the total wetted area, and consequently the surface dissipation.

Figure 10c illustrates the drag polar chart. Clearly, the through-flow nacelles can have a notable impact on the overall changes in C_D, but the three configurations exhibit nearly the same C_L over the operating range of α between $2°$ and $6°$. This result is easier to understand in Table 4, where the variation of drag coefficient with the square of lift coefficient ($\partial C_D / \partial C_L^2$), is presented (induced drag parameter). The lift properties and spanwise load distributions are substantially identical for all the configurations, which means that the BLI and non-BLI configurations have the same vortex dissipation, implying that only propulsion aerodynamic factors contribute to the BLI benefit.

Figure 10d shows the aerodynamic efficiency curves versus lift coefficient. All configurations displayed a similar pattern, where the maximum values were obtained between the interval $0.5 \leq C_L \leq 0.8$, which corresponds to $4° \leq \alpha \leq 6°$. The efficiency curves showed the drag increase produced by the mounted nacelles. Note the aerodynamic performance of the non-BLI and BLI configurations decreased in 8.36% and 3.13%, respectively, when compared to the unpowered configuration. For the sake of argument, it can be concluded that all the aerodynamic measurements were performed successfully, since specific characteristics about the performance of this particular unconventional configuration were observed, such as the soft stall induced by the closed-wing system, and the viscous drag increase caused by the pylon/nacelle interference.

4.2 Power balance and BLI benefit

The outcomes of the integrated systems (non-BLI and BLI configurations) are provided in this section. At Reynolds numbers of 2.72×10^5 and 3.02×10^5, the wheel speed of the propulsors were varied and the net streamwise force and electrical power were measured. The results are shown in Fig. 12, where the net streamwise force coefficient (defined in eq. 2) is plotted against the electrical power coefficient (defined in eq. 5). The crosses represent the points for the seven different runs, and the lines are cubic splines curve-fit through the average of these points at each motor speed (Table 5). Across the entire range of power levels evaluated (Fig. 12a), the BLI configuration required less electrical power for a given net streamwise force than the non-BLI configuration. The BLI benefit (defined in eq. 8) at $C_X = 0$ was found to be $PSC = 7.41 \pm 2.5\%$. Such data were obtained by adjusting the electrical power of the EDFs until the net axial force on the apparatus was zero as measured by the load cell. The data were averaged to evaluate how engine thrust and nacelle installation affected power measurements in non-BLI and BLI configurations. These points can be seen in the zoomed-in view in Fig. 12b. The results are comparable to previous experimental studies that employed the electrical power coefficient instead of the mechanical flow power coefficient. For example, Uranga et al. [34] reported preliminary experimental analyzes of the Double Bubble D8 aircraft with focus on

(a) Full measured range.

(b) Close-up view on $C_X = 0$.
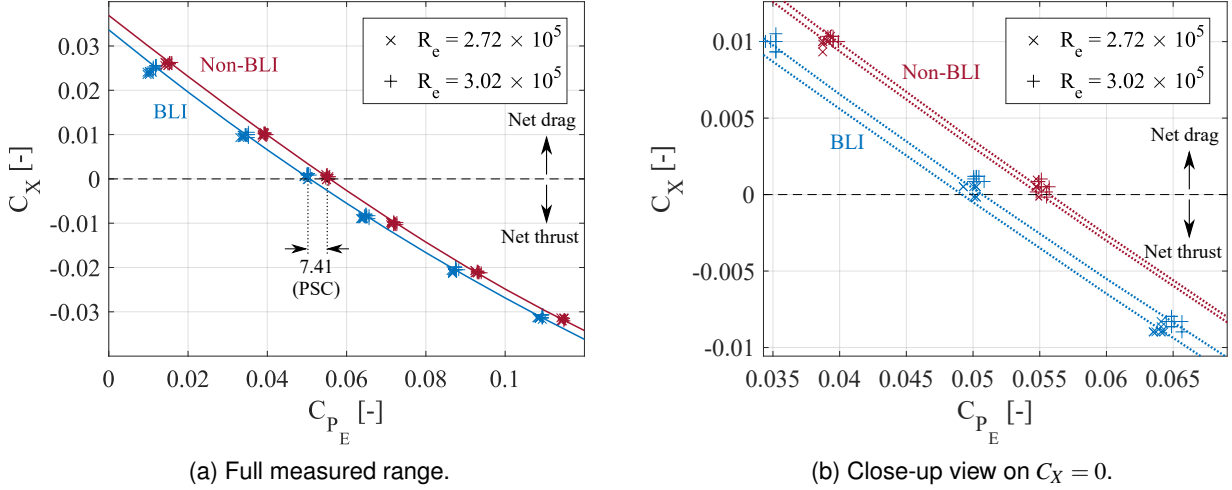
Figure 12 – Net streamwise force coefficient versus electrical power coefficient at $C_L = 0.51$. For each of the configurations, symbols are experimental measurements, and lines are curve fits to data points. Repeatability is $\Delta C_{P_E} = 0.003,\ 0.008$ or equivalently $\Delta C_X = 0.003,\ 0.007$ for non-BLI and BLI configurations, respectively.

Table 5 – Cubic curve-fits of the C_{P_E} versus C_X data.

Tunnel condition	Configuration	Curve Fits and Confidence Interval
$R_e = 2.72 \times 10^5$	Non-BLI	$y = 2.6x^3 + 0.5574x^2 - 0.6947x + 0.03609$; $R^2 = 0.999$
$R_e = 3.02 \times 10^5$	Non-BLI	$y = 3.6x^3 + 0.4454x^2 - 0.6983x + 0.03689$; $R^2 = 0.999$
$R_e = 2.72 \times 10^5$	BLI	$y = 10.8x^3 - 0.989x^2 - 0.5878x + 0.03$; $R^2 = 0.997$
$R_e = 3.02 \times 10^5$	BLI	$y = -0.65x^3 + 1.292x^2 - 0.7276x + 0.03364$; $R^2 = 0.998$

the differences between the BLI and non-BLI configurations at Reynolds number of 3.6×10^5. The authors found a BLI benefit of about $6.85 \pm 2.3\%$. This result is highly comparable to subsequent experiments on this aircraft, in which measurements of pressure fields, velocity magnitudes, and flow directions are used to calculate the mechanical flow power of the propulsors [19]. In the latter case, the measured BLI benefit was $8.6 \pm 1.8\%$ at simulated cruise. Given the experimental uncertainty, the application of the electrical power coefficient under the premise that the motor and fan work near peak efficiencies does not reveal substantial variance, as a positive advantage was found in both experimental campaigns.

On the other hand, CFD simulations using the actual scale and flight conditions of the INTI aircraft demonstrated a power saving coefficient of about 6.52% [25]. This result is not plotted in Fig. 12, because it cannot be compared directly to the power extracted from the wind tunnel experiments. The CFD used an actuator disk model to characterize the propulsors, which does not considered fan rotation. Although the raw experimental data has some uncertainty due to the large degree of interference among the numerous competing effects, it was determined that the studied propulsion system has the potential to provide specific BLI benefits in the order of 5% to 7%.

4.3 Seven-hole probe measurements

According to Uranga et al. [21], three major parameters can influence the BLI benefit: the amount of dissipation ingested by the propulsors; the BLI installation efficiency in terms of surface dissipation reductions; and the propulsor jet velocity (typically set by the propulsor mass flow). As shown in Fig. 12, the variations in P_E between the configurations were derived from changes in the isolated airframe drag values, as well as the propulsion airframe integration effects. This confirms that the BLI benefit depends on the specifics of the integration between propulsor, fuselage, and vertical tail,

(a) Non-BLI configuration.

(b) BLI configuration.
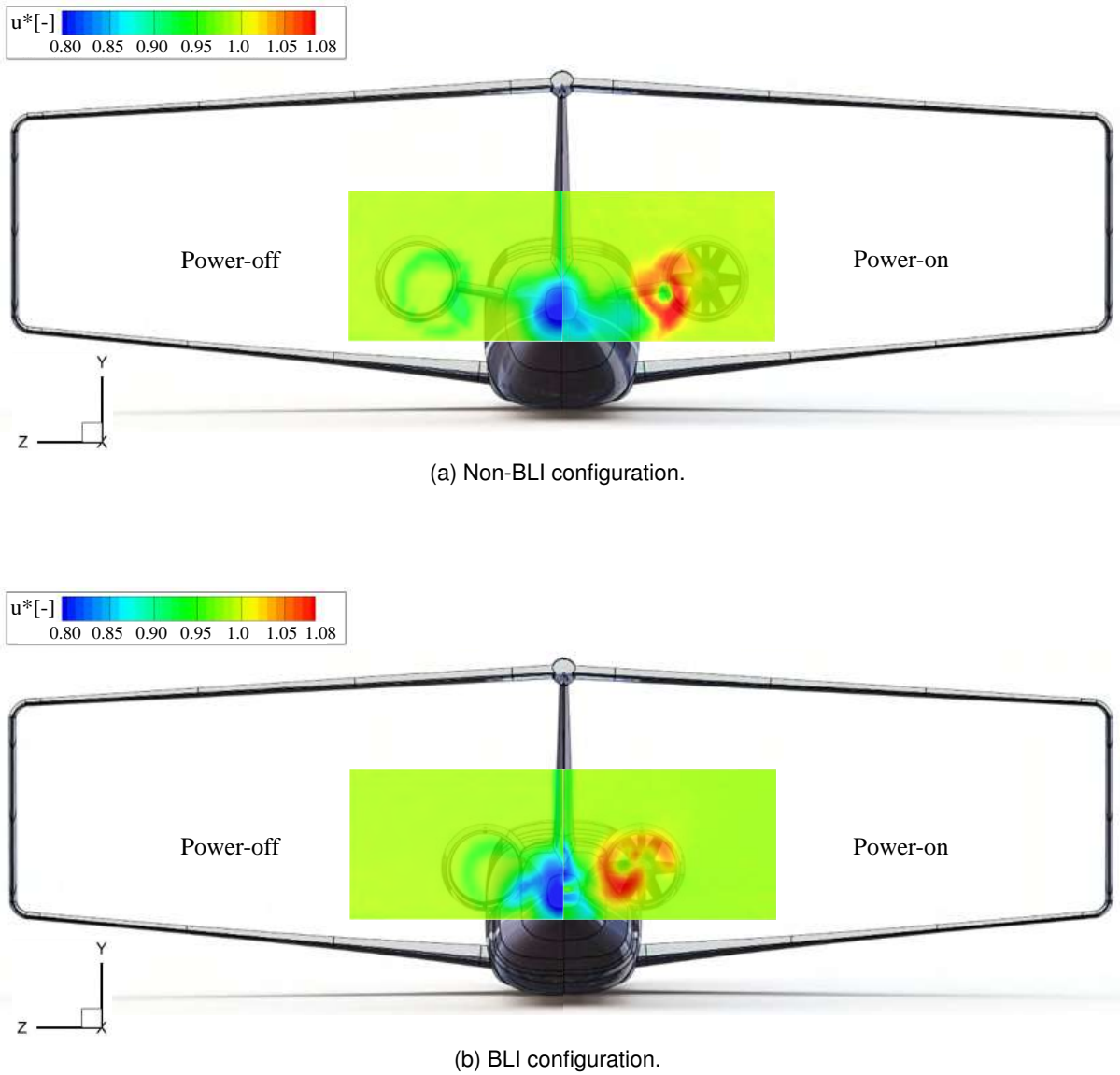
Figure 13 – Axial velocity contours at $R_e = 3.02 \times 10^5$, $C_L = 0.51$, $U_{tip}/V_\infty = 1.96$. Through-flow nacelle condition (left) and powered configurations (right).

achieving reduction in surface dissipation. However, the mechanical flow power, given by eq. 3, is dependent on the total pressure difference and the axial flow velocity, i.e., the streamwise velocity reflects the velocity deficit of the ingested boundary layer. In this context, seven hole probe surveys were conducted as close as possible to the propulsors to investigate the flow-field downstream the aircraft models. The axial velocity and streamwise vorticity were the most relevant flow parameters in the study of the flow-field. Contour maps of velocity (u^*), and streamwise vorticity (ω_x) are shown in Figs 13 and 14, respectively.

The velocity maps (Fig. 13) show the difference between through-flow nacelle condition (left) and powered configurations (right) for non-BLI (Fig. 13a) and BLI (Fig. 13b) configurations, respectively. The contour maps for the u^* component in through-flow nacelle condition revealed regions of reduced velocity, which correspond to the wake and velocity deficit of the airframe. The contour of the non-BLI configuration evidenced a clear aerodynamic interference between the pylon and nacelle, resulting in separation and increased drag on the nacelle's surfaces. At that region, the lowest velocity reached approximately $0.9V_\infty$. In contrast, the contour of the BLI configuration exhibited a larger region of low-velocity fluid due to the incoming boundary layer. In this case, the lowest velocity value reached $0.83V_\infty$. In both cases, the wake from the tail cone has most likely merged, creating a large momentum deficit. On the other hand, the contour maps for the u^* component in powered configurations

18

(a) Non-BLI configuration.

(b) BLI configuration.
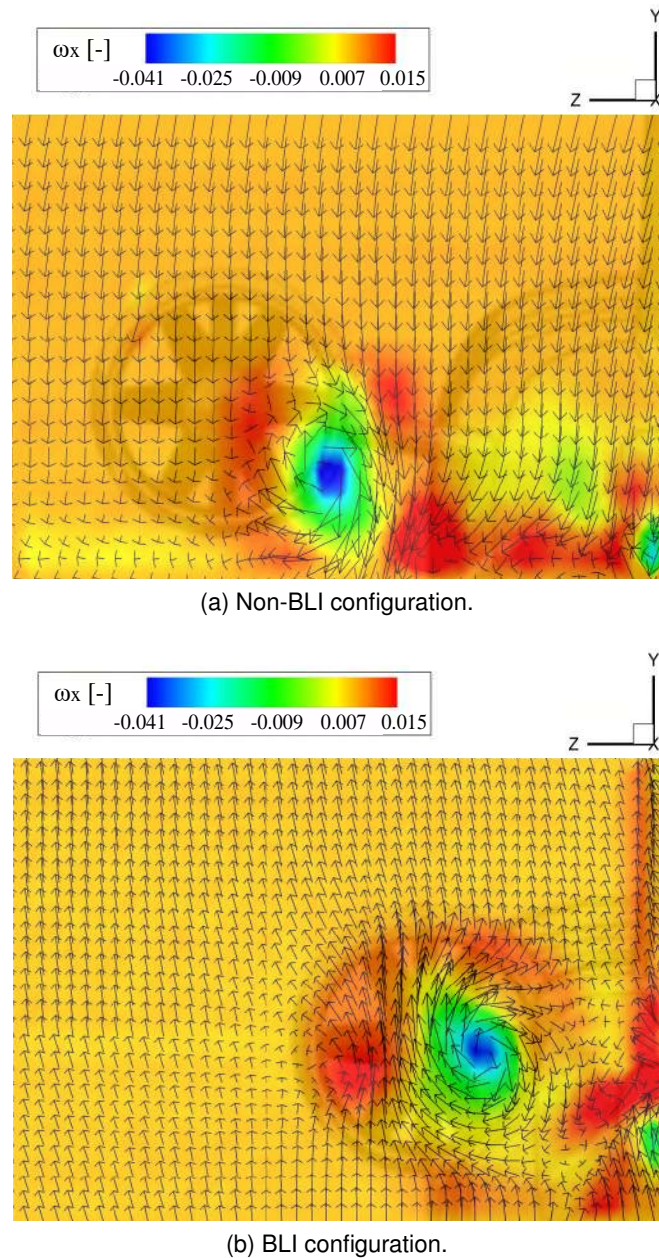
Figure 14 – Close-up views of streamwise vorticity contours and velocity vectors at $R_e = 3.02 \times 10^5$, $C_L = 0.51$, $U_{tip}/V_\infty = 1.96$.

perceived the reduction in kinetic energy dissipation due to the wake and the propulsive jet. Note that the BLI configuration achieved a lower jet velocity ($1.03V_\infty$) than the non-BLI configuration ($1.08V_\infty$), because the exhaust velocities of the BLI propulsor has lower stagnation pressure than the non-BLI propulsor. This result explains the smaller amount of energy (electrical power) of the BLI configuration to reach a certain net streamwise force.

The distributions of axial vorticity along with velocity vectors for the non-BLI and BLI configurations are reported in Figs. 14a and 14b, respectively. Both configurations exhibited a region of negative (clockwise) vorticity at the center, and positive structures along the trailing edges of the nacelles. Such vortical structures also come from the secondary flow resulting of the cross-sectional changes of the different airframes. However, the presence of fans imposed additional complexities, and the vortical structures are the result of the mixing of secondary flows with fan rotational motion. Despite very similar patterns were observed with lower fan voltage inputs, the BLI configuration presented a lower velocity magnitude than the non-BLI configuration when viewed from downstream.

19
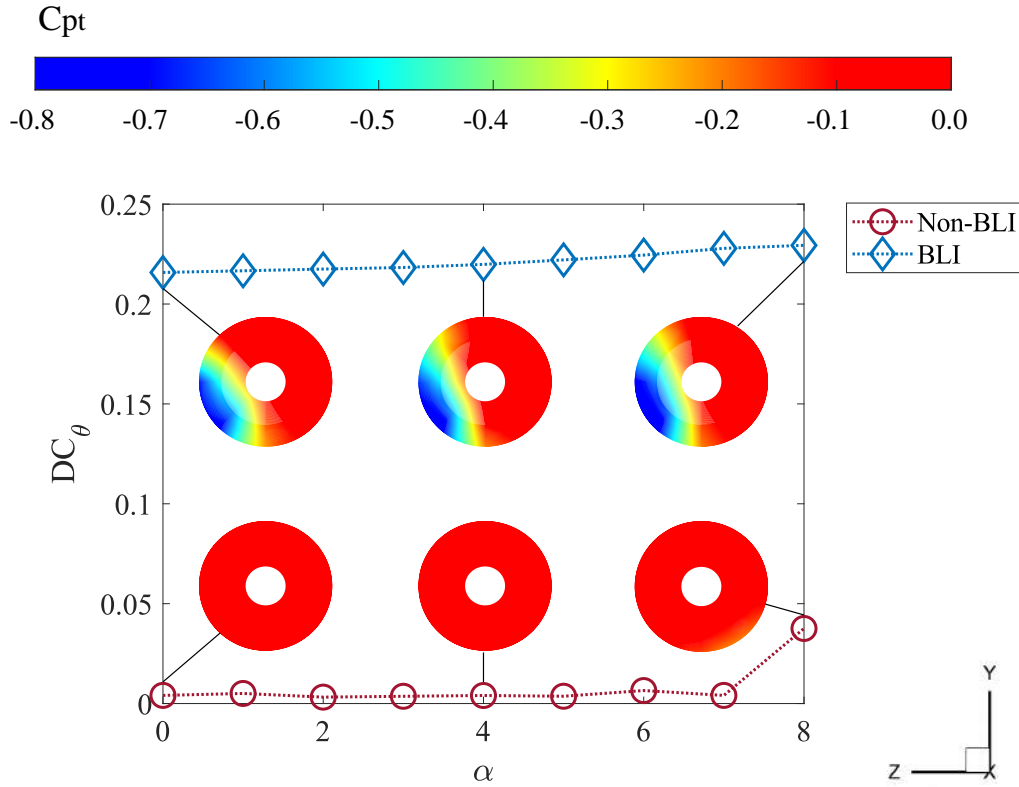
Figure 15 – DC_θ and C_{p_t} experimental results measured on the aerodynamic interface plane at $M = 0.089$, $Re = 3.02 \times 10^5$, and α from $0°$ to $8°$.

4.4 Inlet efficiency

The inflow distortion associated with the fuselage boundary layer is ingested by the inlet duct and delivered to the engine. This fact imposes compatibility challenges due to the effect of the distorted propulsor inflow on fan performance, reducing the overall BLI benefit. To illustrate this issue, the total pressure coefficient contours as well as distortion analysis can be seen in Fig. 15. The grids for the total pressure survey were created using the locations of the probes mounted on the rake (Fig. 8). Therefore, the total pressure coefficient contours were obtained by linearly interpolating in the radial and circumferential directions for grid points between the innermost and outermost points on the survey grid. The values of DC_θ for both configurations and number of runs lie within 1% of each other, confirming the repeatability of the measurements.

The ingested boundary layer can be noted clearly, presenting high indices of distortion, as a consequence of the reduced low-pressure region. However, as the angle of attack increases until $\alpha = 8°$, the performance variation of the BLI configuration is relative low. Note that the pressure distribution seems similar, and the difference in distortion between $\alpha = 0°$ and $\alpha = 8°$ is 5.9%. This indicates that changing the angle of attack has no significant effect on cross-flow or separation in the current engine location, implying that fan performance should be unaffected under several flight conditions. In contrast, an clean airflow is evidenced for the non-BLI configuration until $\alpha = 7°$, however, at higher angles of attack, a small vortex is formed coming in from the side, creating distortion regions of lower total pressure in the aerodynamic interface plane. In sum, the non-BLI configuration presented distortion values of $DC_\theta \sim 0.004 - 0.007$ at low to moderate angles of attack, whereas the BLI configuration had distortion values of $DC_\theta \sim 0.021 - 0.023$, corresponding to total pressure recovery values of $\eta_R = 0.984 \sim 0.977$ and $\eta_R = 0.651 \sim 0.613$, respectively. This indicates that further research is needed to determine the fan response (aerodynamic and aeromechanic) to these higher distortion levels, as well as the influence on engine life cycle.

Finally, mini-tuft flow visualization have been performed upstream and downstream of the nacelles
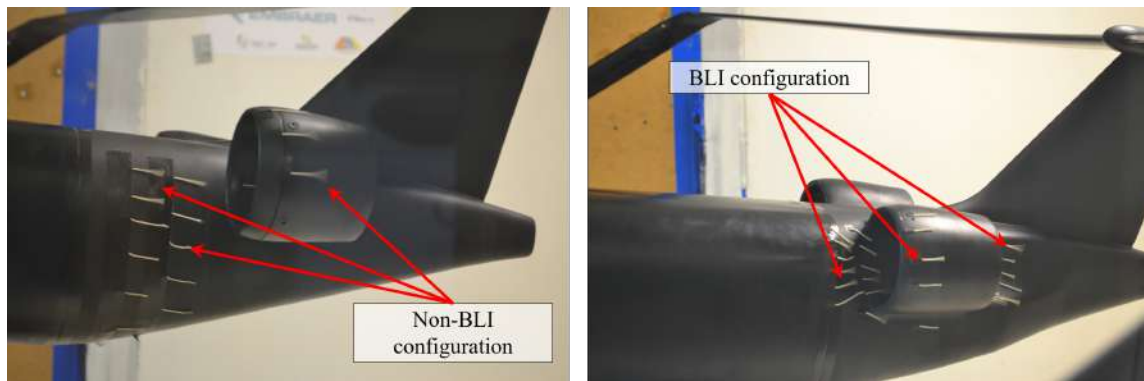
Figure 16 – Mini-tuft flow visualization on fuselage and nacelles upstream of propulsor inlets at $M = 0.089$, $Re = 3.02 \times 10^5$, and $\alpha = 3°$.

to visualize the flow entering the propulsors. The arrange of the mini-tufts at $\alpha = 3°$ is displayed in Fig. 16 for both configurations. Although no large-scale separation can be identified, cross-flow can be seen in both configurations. There are some blurred tufts around the nacelle lips of the non-BLI configuration, indicating a region of accelerated flow. However, the flow far from the propulsors is steady, with the tufts all pointing in the flow direction. In contrast, separated flow can be seen around the incoming flow of the BLI configuration, with tufts pointing in a random direction and continuing inwards and towards the propulsor inlet, i.e., indicating blockage and lower velocity flow entering to the propulsor, which caused high distortion levels. In this case, the overall flow over the nacelles remains aligned to the flow direction. In conclusion, inlet flow distortion is expected to play a major role in unconventional aircraft where complex air induction systems are required to couple the airframe with engines.

5. Conclusions and future work

Wind-tunnel testing of a 3.5%-scale model of the INTI transport aircraft has been performed in the closed circuit wind tunnel at the Laboratory of Aerodynamics of the Aeronautical Engineering Department from São Carlos School of Engineering - University of São Paulo. The investigation presented the use of several methodologies to enable aerodynamic testing over a sub-scale model in order to determine the aerodynamic benefit owing to boundary layer ingestion (BLI). Therefore, it was possible to analyze and validate the main findings during the design process, which are summarized as follows:

- The analyses demonstrated a clear relation between the jet velocity and the power saving coefficient due to BLI, i.e., BLI allows for a lower jet velocity because the ingested flow is slower. As a result, there is a less momentum flow through the propulsor, as well as a more efficient use of power input. The measurements revealed that using BLI saved at least 7.41%±2.5% power in comparison with more conventional free-stream flow ingesting configurations, with a 99% confidence interval. However, due to current scale model limitations, electrical power is used to quantify the BLI benefit, rather than more relevant mechanical flow power measurements of the propulsors. Therefore, subsequent experiments will convert the electrical power into mechanical flow cover by computing the shaft and fan efficiencies. Such experiments will not be difficult because one of the novel aspects of the current work lies in the use of an electrical driven fan, specifically adapted for the needs of the present tests, which allowed to control and measure precisely the power injected into the flow.

- Despite the fact that the current analysis does not explicitly evaluate the BLI benefit for an actual transonic transport aircraft, it does help to validate the processes needed to evaluate the potential of BLI on real aircraft geometries and thus enable their use in the design of novel propulsion technologies that are tightly integrated with the airframe. Indeed, the results of this experiment are similar to those obtained from steady CFD-RANS simulations of an actual scale

and flight condition of the aircraft, although with a $\pm 2.5\%$ margin of error due to aerodynamic modeling uncertainties.

- The results are thought to be useful in understanding BLI aerodynamics for several reasons. First, the fan was scaled to match the full-scale fuselage boundary layer, due to differences in Reynolds and Mach numbers between the wind-tunnel scale and full-scale conditions. Second, the power balance method does not account for differences in Reynolds and Mach numbers, and the benefit of the BLI is mostly attributable to a lower jet to freestream velocity ratio (reduction of around 4.63%) and lower external losses due to the smaller nacelle wetted area (reduction of around 5.62%) compared to the non-BLI configuration. Third, previous research by many authors suggests that compressibility effects are unlikely to have a significant impact on the fuselage boundary layer. This demonstrates how the current aerodynamic model experiment may be used to appropriately assess the aero-propulsive efficiency of a BLI aircraft configuration.

- The aerodynamic flow measurements confirmed the existence of flow distortion which limits the aerodynamic performance of the BLI configuration. Therefore, the specific fan response to the distortion should be the subject of future investigations. This is mostly due to material restrictions, such as dealing with fan-blade stresses caused by the nonuniform incoming flow, which can result in noise or vibration problems.

- A seven-hole probe was used to take the flow measurements. The interference of this probe with the flow should be further investigated, and particle image velocimetry (PIV), a non-intrusive flow measurement technique, can offer a comprehensive assessment of the flow field. Although the findings of this research provide direct evidence for the benefits of boundary-layer ingestion, more research is needed to fully comprehend the influence on aircraft performance in detailed design phases.

6. Contact Author Email Address

mailto: pdbravom@usp.br

7. Copyright Statement

8. Acknowledgments

References

[1] IATA. *IATA Forecast Predicts 8.2 billion Air Travelers in 2037*. Accessed in 23/03/2021. 2021. URL: https://www.iata.org/en/pressroom/pr/2018-10-24-02.

[2] Owen, Bethan, Lee, David S, and Lim, Ling. "Flying into the future: aviation emissions scenarios to 2050". In: *Environmental Science and Technology* 44.7 (2010), pp. 2255–2260.

[3] Hileman, James I et al. "The carbon dioxide challenge facing aviation". In: *Progress in Aerospace Sciences* 63 (2013), pp. 84–95.

[4] Mahashabde, Anuja et al. "Assessing the environmental impacts of aircraft noise and emissions". In: *Progress in Aerospace Sciences* 47.1 (2011), pp. 15–52.

[5] IATA. *Aircraft Technology Roadmap to 2050*. Accessed in 01/03/2020. 2013. URL: https://www.iata.org/contentassets/.

[6] Zingg, David W and Gülder, Ömer L. "Technology Developments and Renewable Fuels for Sustainable Aviation". In: *J Public Health* 21.2 (1997), p. 221.

[7] Graham, William Richard, Hall, Cesare Alan, and Morales, M Vera. "The potential of future aircraft technology for noise and pollutant emissions reduction". In: *Transport Policy* 34 (2014), pp. 36–51.

[8] Bravo Mosquera, Pedro D, Cerón-Muñoz, Hernan D, and Catalano, Fernando. "Design and computational analysis of a closed non-planar wing aircraft coupled to a boundary layer ingestion propulsion system". In: *AIAA Propulsion and Energy 2019 Forum*. 2019, p. 3850.

[9] Greitzer, Edward M et al. "N+3 aircraft concept designs and trade studies, final report". In: *Nasa cr-2010-216794/vol2, NASA Glenn Research Center, Cleveland, Ohio* 44135 (2010).

[10] Drela, Mark. "Development of the D8 transport configuration". In: *29th AIAA Applied Aerodynamics Conference*. 2011, p. 3970.

[11] Wiart, Ludovic and Negulescu, Camil. "Exploration of the airbus "Nautilius" engine integration concept". In: *31st Congress of the International Council of the Aeronautical Sciences*. 2018.

[12] Bowman, Cheryl L, Felder, James L, and Marien, Ty V. "Turbo-and hybrid-electrified aircraft propulsion concepts for commercial transport". In: *2018 AIAA/IEEE Electric Aircraft Technologies Symposium (EATS)*. IEEE. 2018, pp. 1–8.

[13] Seitz, Arne et al. "Concept validation study for fuselage wake-filling propulsion integration". In: *31st Congress of the International Council of the Aeronautical Sciences*. 2018, pp. 09–14.

[14] Hendricks, Eric S. *A review of boundary layer ingestion modeling approaches for use in conceptual design*. Tech. rep. NASA/TM—2018-219926. NATIONAL AERONAUTICS and SPACE ADMIN LANGLEY RESEARCH CENTER HAMPTON VA, 2018.

[15] Bravo-Mosquera, Pedro D., Catalano, Fernando M., and Zingg, David W. "Unconventional aircraft for civil aviation: A review of concepts and design methodologies". In: *Progress in Aerospace Sciences* 131 (2022), p. 100813. ISSN: 0376-0421.

[16] Hall, David K. and Lieu, Michael. "Propulsor Models for Computational Analysis of Aircraft Aerodynamic Performance with Boundary Layer Ingestion". In: *AIAA Scitech 2021 Forum*. DOI: 10.2514/6.2021-0991. eprint: https://arc.aiaa.org/doi/pdf/10.2514/6.2021-0991. URL: https://arc.aiaa.org/doi/abs/10.2514/6.2021-0991.

[17] Menegozzo, Luca and Benini, Ernesto. "Boundary Layer Ingestion Propulsion: A Review on Numerical Modeling". In: *Journal of Engineering for Gas Turbines and Power* 142.12 (2020).

[18] Carter, Melissa B et al. "Designing and testing a blended wing body with boundary-layer ingestion nacelles". In: *Journal of aircraft* 43.5 (2006), pp. 1479–1489.

[19] Uranga, Alejandra et al. "Boundary layer ingestion benefit of the D8 transport aircraft". In: *AIAA Journal* 55.11 (2017), pp. 3693–3708.

[20] Hall, David K et al. "Boundary layer ingestion propulsion benefit for transport aircraft". In: *Journal of Propulsion and Power* 33.5 (2017), pp. 1118–1129.

[21] Uranga, Alejandra et al. "Analysis of the Aerodynamic Benefit from Boundary Layer Ingestion for Transport Aircraft". In: *AIAA Journal* 56.11 (2018), pp. 4271–4281. DOI: 10.2514/1.J056781.

[22] Drela, Mark. "Power balance in aerodynamic flows". In: *AIAA journal* 47.7 (2009), pp. 1761–1771.

[23] Della Corte, Biagio et al. "Power Balance Analysis Experiments on an Axisymmetric Fuselage with an Integrated Boundary-Layer-Ingesting Fan". In: *AIAA Journal* (2021), pp. 1–14.

[24] Della Corte, Biagio et al. "Aerodynamic Performance of an Aircraft with Aft-Fuselage Boundary Layer Ingestion Propulsion". In: *AIAA AVIATION 2021 FORUM*. 2021, p. 2467.

[25] Bravo-Mosquera, Pedro D, Cerón-Muñoz, Hernán D, and Catalano, Fernando M. *Design, aerodynamic analysis and optimization of a next-generation commercial airliner*. Manuscript submitted for publication. 2022.

[26] Catalano, F. "The new closed circuit wind tunnel of the Aircraft Laboratory of University of Sao Paulo, Brazil". In: *24TH International Congress of the Aeronautical Sciencies ICAS*. 2004.

[27] Santana, Leandro Dantas et al. "The update of an aerodynamic wind-tunnel for aeroacoustics testing". In: *Journal of Aerospace Technology and Management* 6 (2014), pp. 111–118.

[28] Almeida, Odenir de, Catalano, Fernando M, and Pereira, Lourenco Tercio. "Improvements of a Hard-Wall Closed Test-Section of a Subsonic Wind Tunnel for Aeroacoustic Testing". In: *International Journal of Acoustics and Vibration* 26.3 (2021), pp. 248–258.

[29] Hantrais-Gervois, Jean-Luc, Piat, Jean-François, and Hantrais, Jean-Luc. "A methodology to derive wind tunnel wall corrections from rans simulations". In: *Integration* (2012).

[30] Barlow, Jewel B, Rae, William H, and Pope, Alan. *Low-speed wind tunnel testing*. John wiley & sons, 1999.

[31] Cerón-Muñoz, H. "Estudo da interferência aerodinâmica do sistema motopropulsor em uma aeronave do tipo BLENDED WING BODY". PhD thesis. São Carlos School of Engineering - University of São Paulo, 2009.

[32] Ceron-Muñoz, HD and Catalano, FM. "Aerodynamic interference of power-plant system on a Blended Wing Body". In: *27TH International Congress of the Aeronautical Sciences, Nice, France*. 2010.

[33] Cerón-Muñoz, HD et al. "Experimental analyses of droop, wingtips and fences on a BWB model". In: *Proceedings of the 30th Congress of the International Council of the Aeronautical Sciences (ICAS 2016), Daejeon, Korea*. 2016, pp. 25–30.

[34] Uranga, Alejandra et al. "Preliminary experimental assessment of the boundary layer ingestion benefit for the D8 aircraft". In: *52nd Aerospace Sciences Meeting*. 2014, p. 0906.

[35] *Aeroprobe L-Shaped Probe*. Accessed in 23/03/2022. 2018. URL: https://www.aeroprobe.com.

[36] *Scanivalve DS4-48 - pressure scanner module, instruction and service manual - by Scanivalve Corp*. 1975.

[37] Frediani, Aldo, Cipolla, Vittorio, and Oliviero, Fabrizio. "IDINTOS: the first prototype of an amphibious PrandtlPlane-shaped aircraft". In: *Aerotecnica Missili & Spazio* 94.3 (2015), pp. 195–209.